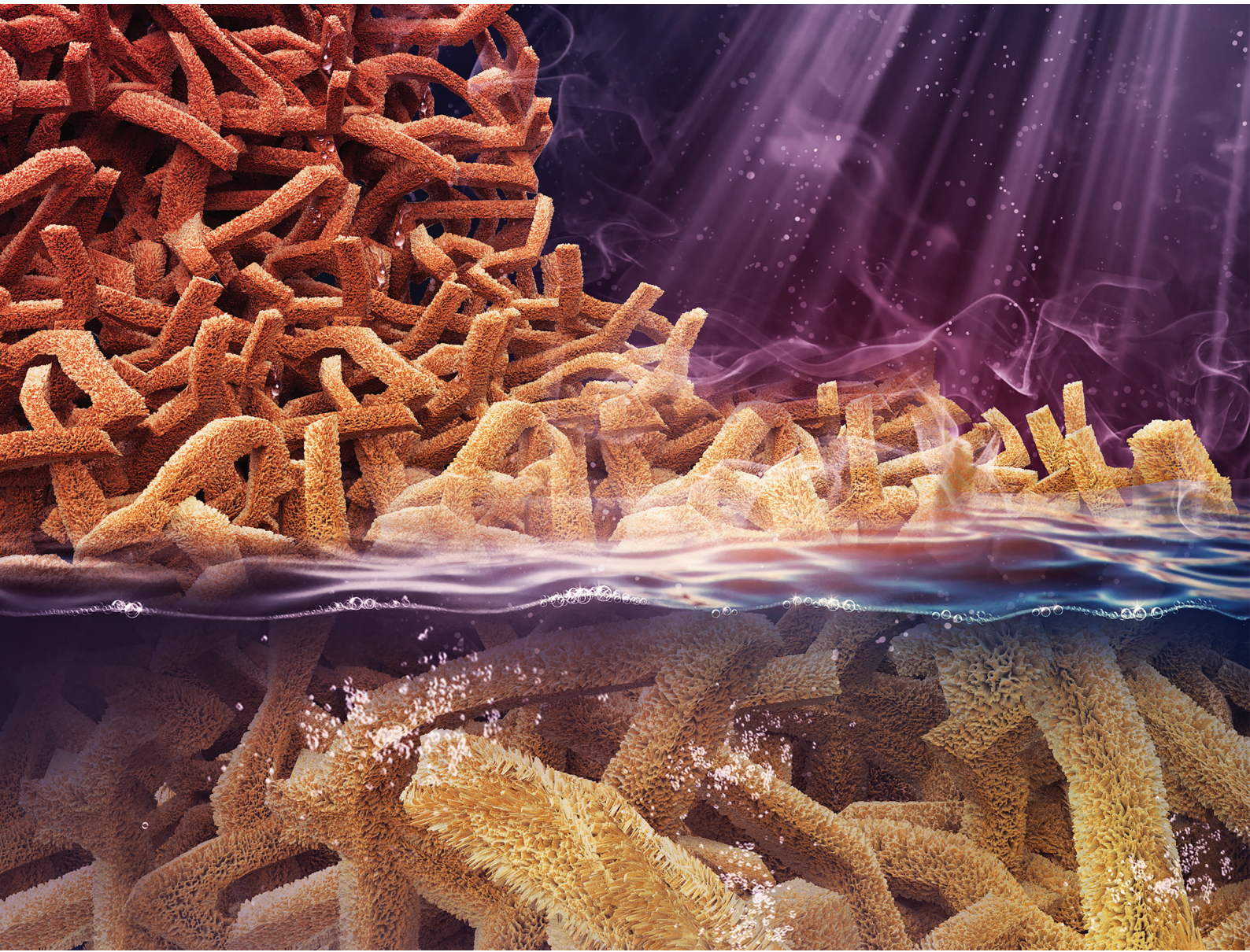


Nanoscale

rsc.li/nanoscale



ISSN 2040-3372



Cite this: *Nanoscale*, 2021, **13**, 17754

Forest waste to clean water: natural leaf-guar-derived solar desalinator†

Andrew Caratenuto,^a Abdulrahman Aljwirah,^a Yanpei Tian,^a Xiaojie Liu,^a Yinsheng Wan^b and Yi Zheng  ^{*a,c}

Water scarcity and waste mismanagement are global crises that threaten the health of populations worldwide and a sustainable future. In order to help mitigate both these issues, a solar desalination device composed entirely of fallen leaves and guar – both natural materials – has been developed and demonstrated herein. This sustainable desalinator realizes an evaporation rate of $2.53 \text{ kg m}^{-2} \text{ h}^{-1}$ under 1 sun irradiance, and achieves consistent performance over an extended exposure period. Furthermore, it functions efficiently under a variety of solar intensities and in high salinity environments, and can produce water at salinities well within the acceptable levels for human consumption. Such strong performance in a large variety of environmental conditions is made possible by its excellent solar absorption, superb and rapid water absorption, low thermal conductivity, and considerable salt rejection abilities. Composed primarily of biowaste material and boasting a simple fabrication process, this leaf-guar desalinator provides a low-cost and sustainable avenue for alleviating water scarcity and supporting a green path forward.

Received 27th July 2021,
 Accepted 13th September 2021
 DOI: 10.1039/d1nr04883j
rsc.li/nanoscale

1 Introduction

At present, multiple grave environmental issues simultaneously threaten human society. For one, an average of 40% of the world population is affected by severe water scarcity annually, driven by both inadequate water quantity and quality.¹ This water insecurity manifests itself not only through human disease and mortality,² but also *via* disruptions to critical operations in agriculture, energy, and transportation.³ In addition, the widespread mismanagement of solid waste products already presents severe consequences to both human and environmental health. The two most commonly utilized solid waste management methods – open burning and open dumping – have dire consequences, including heavy metal pollution in water and plants, the bulk release of harmful atmospheric pollutants, and serious health risks for humans and animal species alike.^{4,5} Such environmental issues have rightfully established themselves as severe global risks, and stand staunchly in the path of sustainable human development.

Methods for obtaining fresh water from saltwater have been implemented to alleviate water scarcity. Reverse osmosis (RO) water desalination is the most widespread technique for obtaining fresh water from seawater, but is a very energy-intensive process typically performed in sizeable facilities.^{6–8} While RO is expanding to developing areas *via* small-scale systems, widespread utilization of this technique in many water-deprived populations is still hampered by high costs and a lack of sufficient energy availability,⁹ and its high energy requirement raises further concerns regarding environmental impact.¹⁰

On the other hand, interfacial solar desalination presents a promising alternative for accessible clean water. Ordinary solar desalination simply heats seawater using incident solar energy to induce vaporization, after which the evaporated liquid is harvested for use.¹¹ In contrast, interfacial solar desalination leverages a porous material, ideally with strong spectral absorptance and water absorbance, to enhance the efficiency of the desalination process, thereby increasing the amount of attainable fresh water from a given system. This porous material floats on the water surface, and is heated by incident solar energy. Simultaneously, water is pumped through the porous structure to the surface *via* capillary pressure. When working in concert, these two behaviors greatly increase the water temperature at the water-absorber interface and expand the total evaporation area, thereby resulting in a more rapid and efficient vaporization process.¹⁰ The process of interfacial solar desalination is shown schematically in Fig. 1a. This concept can be easily applied both with minimal cost and in

^aDepartment of Mechanical and Industrial Engineering, Northeastern University, Boston, MA 02115, USA. E-mail: y.zheng@northeastern.edu

^bDepartment of Biology, Providence College, Providence, RI 02918, USA

^cDepartment of Electrical and Computer Engineering, Northeastern University, Boston, MA 02115, USA

† Electronic supplementary information (ESI) available. See DOI: [10.1039/d1nr04883j](https://doi.org/10.1039/d1nr04883j)

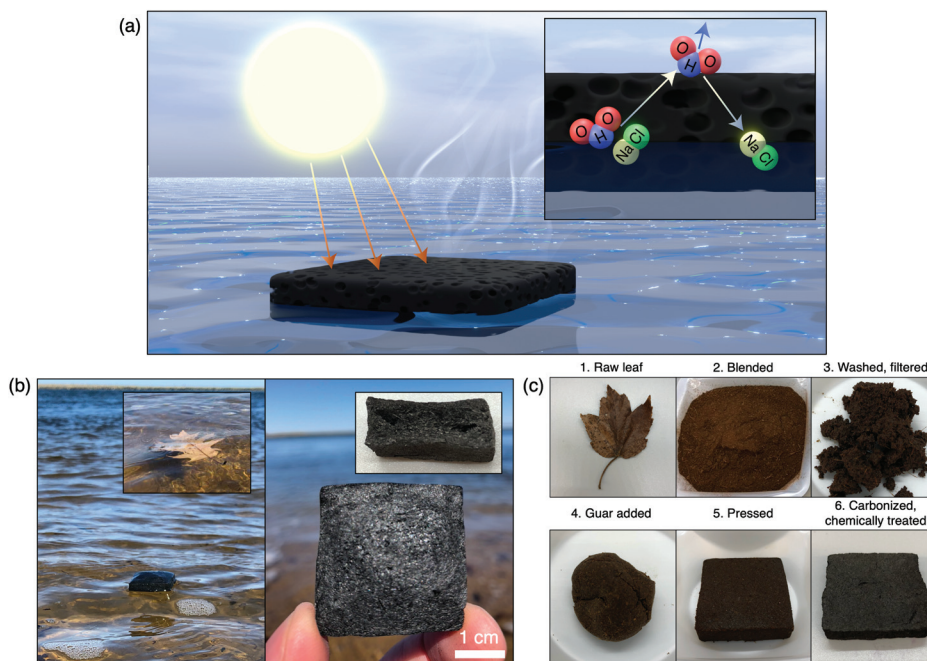


Fig. 1 Qualitative characterization, evaporation mechanism and fabrication process. (a) Schematic illustration of interfacial evaporation mechanism. Desalinator is heated by incident solar radiation, vaporizing saltwater which is pumped to its top surface due to capillary forces. As the water evaporates, the salt is left behind and subsequently rejected back to the bulk water supply. (b) Leaf-guar desalinator floating on ocean water in Newburyport, MA (left) and top view with scale (right). Insets show a raw leaf floating on the same ocean water (left) and cross-sectional porous structure (right). (c) Fabrication process of leaf-guar desalinator: 1. Raw leaves are obtained; 2. leaf stems are removed and leaves are blended down to a fine particle size; 3. leaf particles are rinsed in water and spun for 2 h to enhance particle uniformity and bonding. The wet mixture is filtered overnight to remove excess water; 4. guar is mixed into the filtered leaf by hand to add stability to the mixture; 5. the leaf-guar mixture is hand-pressed in a mold to compress it and define its shape. Approximately 0.5 mm of material is removed from the side walls with a razor blade to better expose the inner porous structure; 6. The leaf-guar mixture is carbonized in a vacuum furnace for 1 h at 500 °C, after which it is treated in a HNO₃ solution for 2 h at 65 °C to enhance water absorption.

remote areas which lack reliable energy access, providing cheap, effective water access to underdeveloped communities and for disaster-related scenarios.¹²

Interfacial solar evaporation owes its high efficiency to the porous absorber floating on its surface (herein referred to as the desalinator), so the effectiveness of the desalinator is of primary significance to these systems. Several key desalinator properties, such as strong solar absorptance, low thermal conductivity, great water absorbance, and effective salt rejection capabilities, all contribute greatly to a high-performing solar desalinator.^{12,13}

Many desalinators which boast these key characteristics have been designed, possessing highly efficient vaporization capabilities. Using materials such as polydimethylsiloxane (PDMS),¹⁴ iron oxides,¹⁵ and polyimide (PI),¹⁶ strong evaporation and reliability performances have been achieved. While these materials do possess strong desalination abilities, alternatives composed of natural materials would result in far less stress on the parallel waste mismanagement crisis. Some emerging desalinators make use of organic raw materials (often carbonizing them to enhance their photothermal absorption and structural properties), representing a substantial step towards a sustainable future by alleviating both water scarcity and waste mismanagement issues.¹⁷ However, some of

the natural materials utilized – wood,¹⁸ cotton yarn,¹⁹ and mushrooms,²⁰ for example – are frequently utilized in other business sectors such as building materials, clothing, or agriculture, and therefore possess a non-negligible value to these industries. That being said, an ideal desalination solution would instead be primarily comprised of a bio-waste material, presenting both a minimal raw material cost and a minimal environmental impact.

Such a biowaste-derived desalinator, composed of fallen maple tree leaves and guar powder, is detailed herein and shown in Fig. 1. Fallen leaves are dominantly characterized as forest/residential/urban wastes, often collected and hauled to landfills or burned – management strategies which present obvious environmental and monetary ramifications.^{21–23} However, leaves consist mainly of cellulose, hemicellulose, and lignin, and as such can be easily carbonized *via* high-temperature thermal treatment^{24,25} to enhance solar absorption.¹⁷ In addition, their intrinsic structures already consist of porous channels which can aid water absorption.^{17,24}

Because raw leaf particles alone demonstrate extremely poor structural stability when carbonized, guar powder is added to the desalinator to promote structural stability. Guar is derived from the seeds of the legume *Cyamopsis tetragonoloba*. It is primarily composed of the sugars galactose and

mannose, and is used often as water-soluble thickening agent in food products.²⁶ This hybrid leaf-guar desalinator naturally absorbs the majority of incident solar irradiance at a wide range of incidence angles, and effectually retains this heat during use as a desalinator owing to its low thermal conductivity. After a one-time treatment in a nitric acid (HNO_3) solution, the material also displays rapid water absorption and strong salt-rejection behaviors. These desalinator characteristics work in concert to achieve a single-hour evaporation rate of $2.53 \text{ kg m}^{-2} \text{ h}^{-1}$ under 1 sun, as well as a 12 h averaged evaporation rate of $2.40 \text{ kg m}^{-2} \text{ h}^{-1}$ under the same irradiance. Even when applied to saline solutions with concentrations as high as 10% by weight, there is no salt accumulation on the top surface of the desalinator. Comprised entirely of environmentally inert materials, boasting a highly efficient evaporation rate and demonstrating long-term reliability, this desalinator repurposes biowaste to simultaneously alleviate the global water scarcity and waste mismanagement crises without the burdens of high cost or complex fabrication methods.

2 Experimental methods

2.1 Materials

Fallen maple tree leaves were gathered at Lincoln Woods State Park, Rhode Island. Guar, NaCl (99.0%), and HNO_3 (70%) were obtained from Sigma-Aldrich.

2.2 Fabrication process

The fabrication process of the leaf-guar desalinator is shown visually in Fig. 1c. First, raw leaves are harvested. Leaf stems are removed, while the remainder of the leaves are blended for 30 seconds to obtain a fine particle size. The blended leaf particles are rinsed in water and spun for 2 h at 500 rpm to enhance particle uniformity and bonding ability. The wet leaf-water mixture is filtered overnight (roughly 18 h) to remove excess water and obtain a saturated mixture. Guar is mixed into this mixture by hand to add stability to the mixture, at a ratio of 1 g of guar to 9 g of saturated leaf-water mixture. 20 g of the leaf-guar mixture is hand-pressed in a $45 \text{ mm} \times 45 \text{ mm}$ mold to compress it and define its shape. Approximately 0.5 mm of material is removed from the side walls with a razor blade to better expose the inner porous structure. The leaf-guar mixture is placed in an oven at 60°C for 24 h, then carbonized in a vacuum furnace for 1 h at 500°C . A 500 g mass is placed on top of the sample during carbonization to apply a compressive force, used to achieve relatively smaller pore diameters and a more homogeneous internal porous structure. After carbonization, a solution of HNO_3 and water at a ratio of 1 g HNO_3 to 5 g water is prepared. This solution is raised to 65°C and covered with plastic wrap to prevent evaporation of the solution. The carbonized sample is treated in the solution under magnetic stirring at 800 rpm for 2 h to enhance water absorption.

It should be noted that the guar was added to enhance the structural stability of the desalinator. Upon carbonization at

various temperatures ranging from 300°C to 800°C , the filtered leaf mixture alone was reduced to an ashy substance with very little structural stability. The carbonized leaf would fall apart when handled, making it unsuitable for use as a desalinator (Fig. S1†). In contrast, when the guar is added prior to carbonization, the desalinator displays excellent structural stability, capable of withstanding sizeable compressive loads on its top and side faces (Fig. S2†).

In addition to this final version of the leaf-guar desalinator sample, samples were also prepared at various stages of the fabrication process to enable comparison and illustrate the importance of each fabrication step. Raw samples were fabricated by pressing 20 g of the filtered leaf mixture (without adding guar) into shape, and subsequently drying them at 60°C for 24 h. Uncarbonized samples were prepared by following all fabrication steps up until carbonization, and untreated samples were prepared by following all fabrication steps up until the chemical treatment. While the recyclability of finalized samples is not studied in the context of this work, recyclability with comparable carbonized natural materials has been demonstrated.²⁷ Similar methods are expected to be easily applicable to the leaf-guar material based on material and fabrication method similarities.²⁷

2.3 Material characterizations

Absorbance data (300–2500 nm) was obtained by measuring the reflectance spectra of samples with the Jasco V770 spectrometer, using the Jasco ISN-923 integrating sphere at an angle of 6° . As samples are opaque, transmittance was assumed to be zero, and absorbance was obtained by subtracting the reflectance values from 1. The normalized absorbance values at various angles of incidence were obtained using the same equipment with the addition of angled wedges to modify the incidence angles. The FTIR transmissivities were obtained using the Jasco FTIR 6600. Thermal conductivities were measured using the HotDisk TPS 2500s. Porosities were measured by analyzing the SEM images using ImageJ. High-speed camera images were obtained from the Chronos 2.1-HDcamera. The contact angle measurement was performed using the SINDIN SDC-350 contact angle meter. SEM images were obtained using the Supra 25 SEM at an acceleration voltage of 5 kV. Chemical surface characterizations were performed using the Bruker Quantax EDS under an acceleration voltage of 15 kV. All samples were coated with 10 nm of a gold/palladium mixture prior to imaging with the SEM and EDS characterization. Temperature data and thermal camera images were taken using the FLIR A655C thermal camera with a resolution of 640×480 using a 25° lens. Evaporated water salinity was evaluated using the Extech EC400 ExStik salinity meter. The three-point bending test was performed with a gap of 10 mm using the TA Instruments RSA-G2 at a rate of 0.01 mm s^{-1} .

2.4 Solar evaporation rate experiment

The evaporation rate and desalination experiments employed the Newport 94801a solar simulator to drive evaporation. The

distance between the desalinator top surface and the solar simulator optical lens was set to apply a solar irradiance of 1000 W m^{-2} to the desalinator. This value was verified using the TES 132 Solar Power Meter before each experiment to confirm the irradiance value. For other solar irradiance values employed for the solar output variation tests, the power of the solar simulator was adjusted, and the irradiance was also measured using the same solar power meter prior to the experiment. The mass of water was measured using the RADWAG PS 1000 electronic scale, with a resolution of 0.001 g. These experiments were conducted in the laboratory under ambient conditions (20°C , 1 atm).

3 Results and discussion

3.1 Material properties

Fig. 2 and S3[†] illustrate the mechanical, material and spectral properties which enable the leaf-guar desalinator to function as a highly effective water evaporation device. The treated sample is extremely stable in water, showing no visible degradation after extended exposure to water (Fig. S3 and S4[†]). In contrast, the uncarbonized form of this sample begins to degrade in water within 10 min, and the raw sample demonstrates even less resistance to diffusing into the water. The sample also shows excellent mechanical stability in response

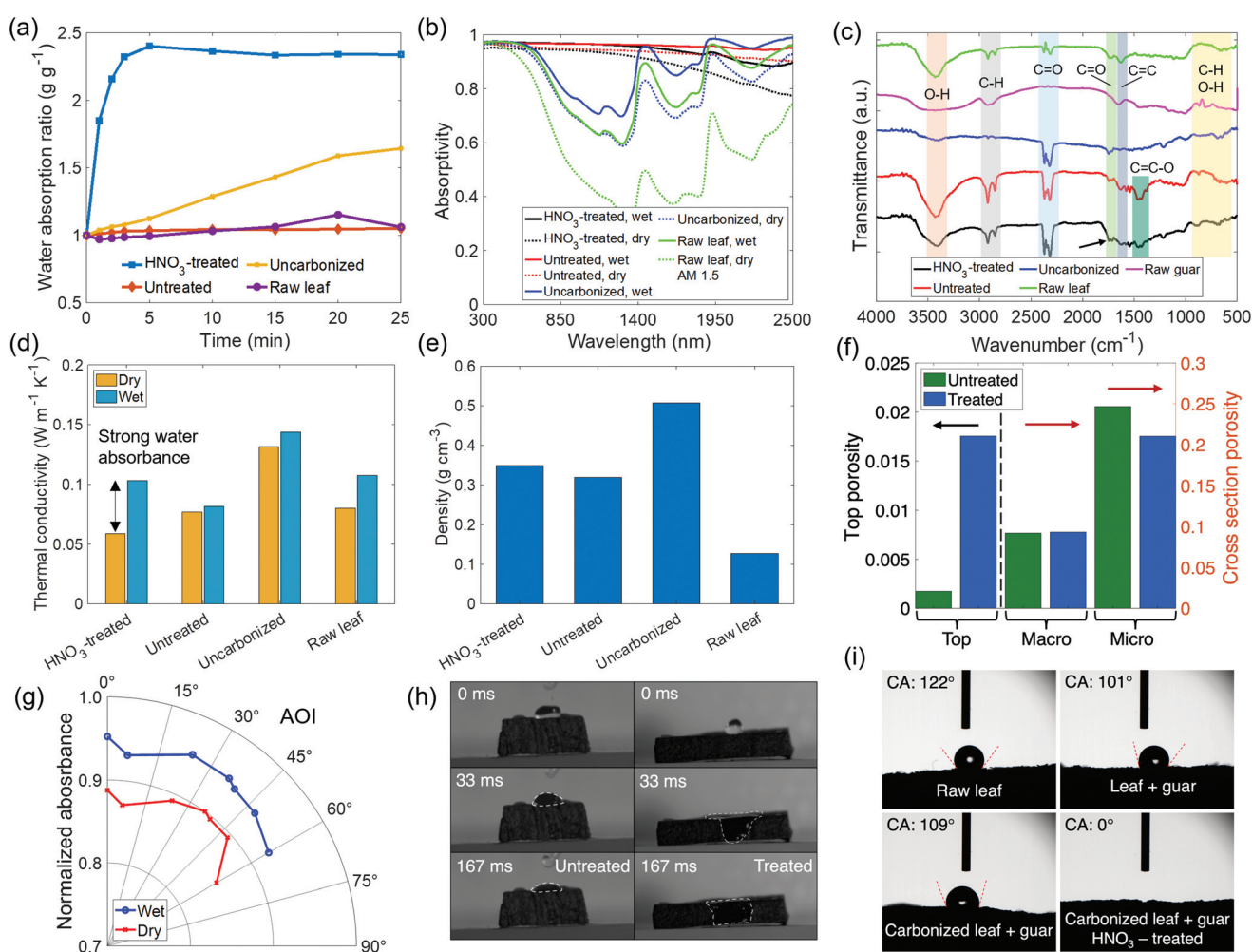


Fig. 2 Desalinator characterizations. (a) Water absorption ratio of leaf-guar desalinator compared with samples at other stages in the fabrication process (untreated desalinator, uncarbonized desalinator, and raw leaf sample (without guar)). (b) Visible and near-IR absorbances of leaf-guar desalinator versus those of samples at other fabrication stages, all in both wet and dry states. The normalized 1.5 air mass solar irradiance spectrum is shown for comparison. (c) FTIR transmittance spectra of leaf-guar desalinator, as well as samples at other fabrication stages. (d) Thermal conductivities of leaf-guar desalinator versus samples at other fabrication stages, in both wet and dry states. (e) Dry densities of leaf-guar desalinator compared with samples at other steps in the fabrication process. (f) Top surface, macro-scale, and micro-scale porosities of untreated and treated leaf-guar desalinators. Arrows denote the respective axes for each group of measurements. Unit depth is assumed to calculate the porosity. (g) Spectral absorption of wet and dry leaf-guar desalinators at various angles of incidence, normalized with respect to the solar irradiance spectrum in the wavelength range of 300–2500 nm. (h) High-speed camera images capturing the lack of water absorption for the untreated desalinator (left) as well as the rapid water absorption for the treated desalinator (right). (i) Contact angle measurements for leaf-guar desalinator samples at various stages of the fabrication process.

to three-point bending, with a fracture stress of over 600 kPa (Fig. S5†). This greatly enhances the ease of handling and real-world feasibility of this design. The water absorption of this leaf-guar-derived desalinator is relatively quick, with the sample reaching its fully swelled state in less than 5 min, as shown in Fig. 2a. In addition, the sample is able to absorb nearly 150% of its original mass at peak capacity. While the uncarbonized sample does display fair water absorption, its long-term stability in water is inadequate. On the other hand, the untreated sample is stable in water, but displays barely any water absorbance. This sample does have a well-defined internal porous structure (Fig. 2f) brought on by pyrolysis. However, the untreated sample also displays a low polar surface energy typical of activated carbon structures^{19,28} which limits its water absorption capabilities. The chemical treatment remedies this by both increasing the surface oxygen content and by generating macropores on the surface,²⁸ resulting in a greatly enhanced water absorption performance for the treated sample.

In addition to strong water absorbance, the leaf-guar desalinator also displays extremely strong spectral absorbance. At an incidence angle of 6 degrees, as shown in Fig. 2b, the wet desalinator maintains an absorbance well over 0.9 across nearly the entire range of solar radiation. The performance is slightly worse in its dry state, which is largely inconsequential considering its intended application as an absorbent evaporator floating on water. Both the treated and untreated carbonized samples show much stronger spectral absorbance curves over the solar wavelength region than the uncarbonized samples, as expected based on the known spectral absorbance benefits for many natural materials due to carbonization.¹⁷ Specifically, spectral absorption in the near-infrared region experiences the greatest benefit from the carbonization process. In addition, the spectral absorbance of the desalinator is largely angle-independent (Fig. 2g), retaining wet absorbance values well over 90% at incidence angles as high as 60 degrees when normalized with respect to the AM 1.5 solar irradiance data.²⁹

Fig. 2c provides insight into the chemical bonds present within the various desalinator fabrication stages, as well as the raw guar. Many of the spectra peaks occur at similar locations, indicating similar bond structures through the fabrication process. All materials display peaks near 3450 cm^{-1} , 2850 cm^{-1} , and 2350 cm^{-1} , corresponding respectively to the hydroxyl group (O-H), C-H stretching vibrations, and C=O stretching vibrations.³⁰⁻³³ There are also a variety of vibrations due to C-H and O-H groups in the $900\text{--}600\text{ cm}^{-1}$ range,³⁰⁻³⁵ though their intensity is lesser compared with other peaks. In addition, a C=C band is notable amongst all materials with relatively comparable intensity near 1650 cm^{-1} .³⁰⁻³³ Two notable spectral differences are apparent through the various fabrication stages: the emergence of the peak near 1450 cm^{-1} after carbonization, as well as the increase in the peak near 1700 cm^{-1} after the chemical treatment. The former of the two is attributed to the formation of C=C-O groups as a result of the breakdown of organic compounds (such as benzene) at the carbonization temperature³¹ as well as the increase in oxygen

levels introduced from the pyrolysis process.²⁸ The latter peak increase near 1700 cm^{-1} (black arrow) is due to increases in surface oxygen levels due to the chemical treatment.²⁸ The enhancement of surface oxygen levels brought on by the chemical treatment is corroborated using energy dispersive spectrometry (EDS) to characterize the proportions of elements on the sample surfaces. Prior to the HNO_3 treatment, the surface of the carbonized sample contains roughly 20% oxygen by mass. After this treatment, the surface oxygen levels increase to over 27%, illustrating a notable change in the surface oxygen levels of the sample and aiding water absorbance as a result. In addition, the surface oxygen distribution of the treated sample is far more uniform, providing more consistent absorbance performance. These results are shown in Fig. S6.†

Fig. 2d illustrates how the leaf-guar desalinator fulfills the low thermal conductivity requirement necessary for strong evaporation performance. Samples in all fabrication stages display relatively low thermal conductivities, attributable to the low electrical conductance of cellulose-heavy materials.³⁶ In addition, the carbonized structures have even lower thermal conductivities than the uncarbonized structures, brought on by the porous structure that emerges after carbonization which introduces air gaps to the internal structure,³⁷ as is seen in Fig. 3. Relative to its dry state, the wet desalinator does experience a notable rise in thermal conductivity in its soaked state. This is a result of the absorbed water present in the structure, raising its thermal conductivity closer to the value of water.³⁷ Even so, this wet thermal conductivity is still extremely low, and helps to limit heat loss to the bulk water supply during operation.

The density and porosity of various samples are displayed in Fig. 2e and f, respectively. Porosity is determined by treating the SEM images of the desalinator cross-section as a representative average of the internal structure. The carbonization process greatly reduces the density of the samples, in part due to the introduction of the porous structure. The internal porosities of the carbonized samples remain largely unchanged before and after the chemical treatment. However, there is a significant change in the top surface porosity which allows water to penetrate the sample surface down to the internal porous structure, greatly enhancing the water absorption of the treated sample. The impact of this chemical treatment is further elucidated in Fig. 2h and i. The high-speed camera images show that while the untreated sample does not appear to absorb any of an interfacing water droplet after 167 milliseconds, leaving the entire drop on its surface, the treated sample is observed to absorb the droplet nearly immediately. Further high-speed images are included for raw and uncarbonized samples in Fig. S7.† In addition, the contact angle measurement in Fig. 2i strongly supports the data of Fig. 2a. All samples besides the treated one resist water absorption, made clear by their large contact angles, while the treated sample absorbs water immediately, with a contact angle of zero.

The SEM images (Fig. 3) clearly display the microscopic changes brought on by both the carbonization and chemical treatment processes. While the uncarbonized sample does not

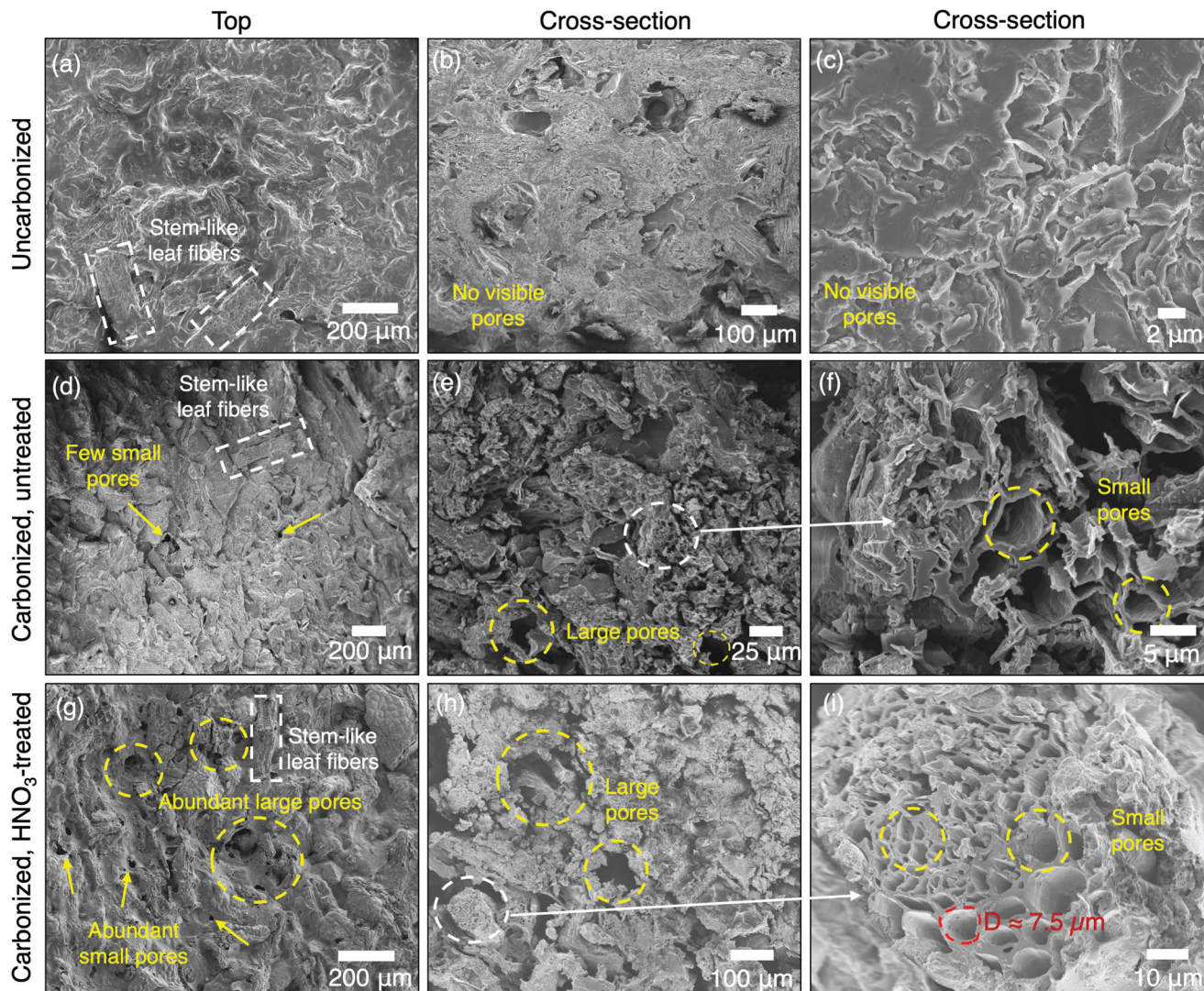


Fig. 3 Surface characterizations of leaf-guar desalinator. SEM images of uncarbonized sample (a) top view and (b and c) cross-section view. SEM images of carbonized, untreated sample (d) top view and (e and f) cross-section view. SEM images of carbonized, treated sample (g) top view and (h and i) cross-section view. The figure illustrates that the uncarbonized sample lacks the porous structure of the carbonized samples, in addition to the fact that the chemical treatment greatly increases the top surface porosity, thus allowing for increased water absorption.

display pores on its top surface nor in its internal structure, both the untreated and treated carbonized samples have very obvious pores. Material decomposition and volumetric shrinkage are the main drivers of pore formation during the carbonization process.⁴² As indicated earlier *via* Fig. 2f, the cross-sectional porosities of both untreated and treated carbonized samples are very similar. However, the chemical treatment greatly increases the top surface porosity, allowing for significantly more water absorption.

3.2 Desalination performance

The leaf-guar desalinator displays consistent evaporation performance under 1 sun of irradiation even after long-term use. The desalinator evaporation rate testing setup is schematically illustrated in Fig. 4b. The sample is placed within aplastic

beaker of DI water, held in contact with the top water surface using a tight-fitting piece of 12.7 mm-thick polyethylene (PE) foam. The foam also prevents evaporation effects that are not due to interfacial interactions with the desalinator. With a measured thermal conductivity of $0.068 \text{ W m}^{-1} \text{ K}^{-1}$, the foam inhibits heating of the bulk water by the solar simulator and simultaneously produces a tight seal with the beaker to restrict water outflow from the outer beaker edge. This beaker is placed on an electronic scale, while the solar simulator is used to supply 1 sun (1000 W m^{-2}) of irradiation to the top sample surface. The solar output is verified with a solar intensity meter. As the sample heats up, water in contact with the desalinator begins to evaporate, and the associated mass changes are recorded over time and used to calculate the evaporation rate. In Fig. 4a, the individual and averaged evaporation rates

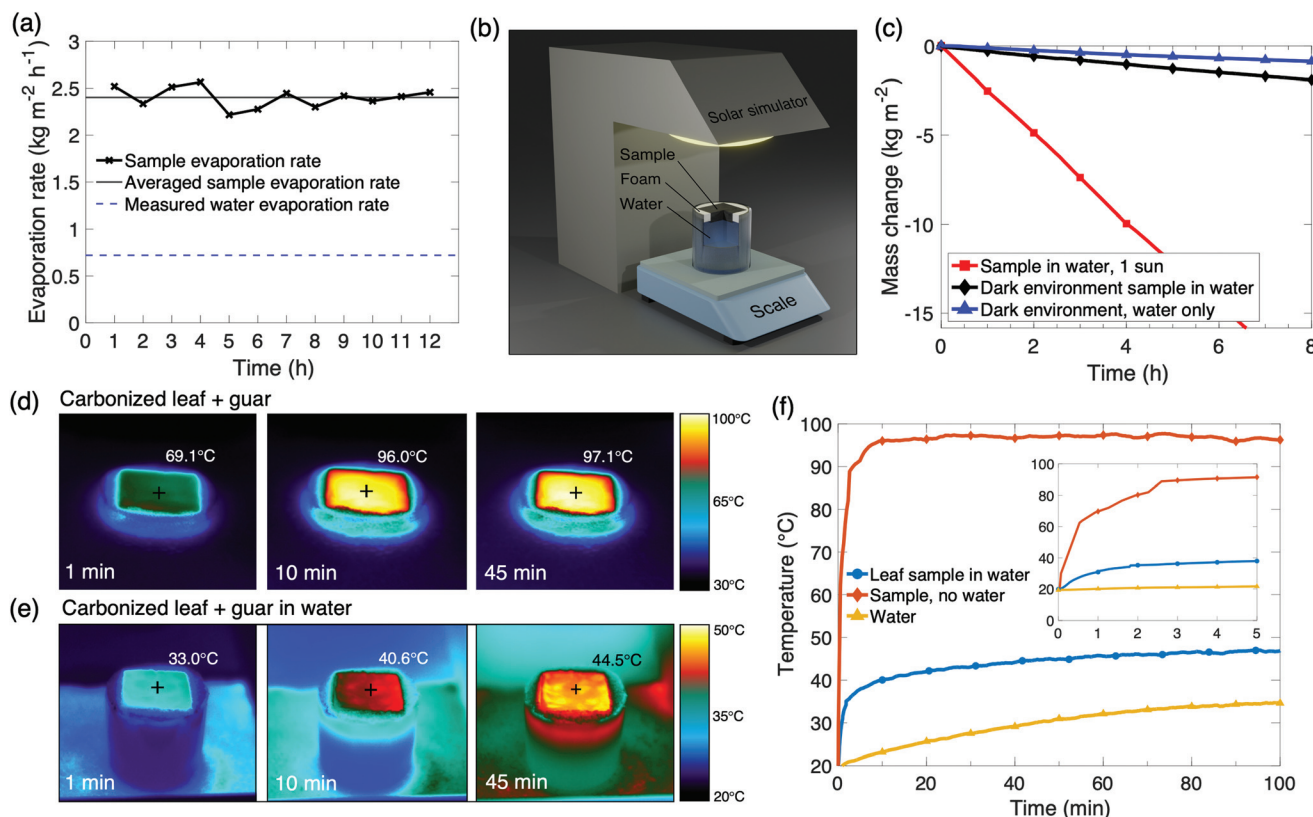


Fig. 4 Evaporation rates and thermal responses. (a) Hourly evaporation rates of leaf-guar desalinator for long-term use under 1 sun irradiation. Four extended trials of 3.5 h each were performed, with the evaporation rate calculation beginning after the first 30 min. The sample displays relatively consistent performance as an efficient desalinator, far exceeding the evaporation rate of water alone. (b) Schematic of experimental setup used for solar desalination testing. (c) Long-term mass changes of the leaf-guar desalinator in water under 1 sun, as well as dark environment mass changes for the desalinator and pure water. Thermal camera images of (d) the desalinator alone and (e) the desalinator on the water surface at various times under 1 sun. (f) Temperature responses of the desalinator alone, the desalinator on the water surface, and pure water under 1 sun. The associated inset displays the first five minutes of data to illustrate the rapid thermal response of the desalinator.

over 12 h are obtained from four 3.5 h trials, with the first 30 min of data being set aside in order to obtain a consistent solar flux. The first hour of this experiment yields an evaporation rate of $2.53 \text{ kg m}^{-2} \text{ h}^{-1}$, with an average rate of $2.40 \text{ kg m}^{-2} \text{ h}^{-1}$ over the entire 12 h period – more than three times the measured evaporation rate of water alone tested under identical conditions. This performance far exceeds that of other biomass-derived evaporators with comparable fabrication methods presented in recent literature, as seen in Table 1. Fig. 4c displays the consistent level of mass change over a 6 h period, indicating the stability of the leaf-guar desalinator for

a long-term application. In a dark environment at ambient temperature and pressure (20°C , 1 atm), the rate of mass change from the desalinator is significantly greater than that of pure water. This results in a lower evaporation enthalpy for the sample as compared with water, indicating that the evaporation efficiency of the leaf-guar desalinator is greater than that of water alone.⁴³

Fig. 4d and e elucidate both the excellent solar absorbance and rapid water transport of this desalinator. Under an irradiance of 1 sun, the desalinator rises from the ambient temperature of 20°C to nearly 70°C in one minute, and reaches its

Table 1 Comparison of recent all-biomass desalination device performances

Material	Fabrication method	Evaporation rate (1 sun) ($\text{kg m}^{-2} \text{ h}^{-1}$)
Rice straw ³⁸	Freeze drying + carbonization	1.20
Mushroom ²⁰	Carbonization	1.48
Towel-gourd ³⁹	Carbonization	1.53
Loofah ⁴⁰	Carbonization	1.72
Carbon fiber + cotton yarn ¹⁹	Weaving	1.87
Basswood ⁴¹	Hydrothermal treatment + carbonization	2.20
Leaf + guar (this work)	Carbonization	2.53

peak temperature within about 10 min. This short ramp-up time is critical for a solar desalinator, as it allows full advantage to be taken of daily sunlight. Furthermore, when water is supplied to the desalinator, the peak temperature drops by roughly 50 °C as the consistent water supply cools the device through convective heat transfer as the colder water flows through the internal porous structure. This further emphasizes the excellent water transport abilities of this desalination device.

While a strong evaporation performance in pure water has been demonstrated, an ideal desalinator must also exhibit comparable performance in a variety of environmental conditions. Incident sunlight may vary by hour or by day in practice, so a reliable desalinator must conform to these conditions while still outputting the maximum quantity of evaporated water. In Fig. 5a, the performance of the leaf-guar desalinator is shown under a variety of irradiation levels common for clear and cloudy days.⁴⁴ Under an irradiation of 1.2 suns, the leaf-guar desalinator evaporation rate rises to $3.25 \text{ kg m}^{-2} \text{ h}^{-1}$, a highly efficient performance which shows that the aforementioned key desalinator characteristics scale with an increased thermal input. At lower irradiation values of 0.8 and 0.6 suns, the desalinator performance drops below $2.00 \text{ kg m}^{-2} \text{ h}^{-1}$, as is expected due to the reduced energy input. However, the desalinator does not see a steep performance

decline; rather, the performance drop between all intervals is nearly consistent, indicating its usefulness as a solar desalination device even in cloudy environments.

As the leaf-guar desalinator is intended to produce clean water from salt water, characterizing the evaporation performance in various saline solutions is essential. When the DI water is replaced with a salt water solution, the performances of solar desalinators tend to suffer due to the accumulation of crystallized salt within the water pathways.¹⁷ While this trend is apparent within this work, the leaf-guar desalinator still displays an exemplary evaporation rate of $2.09 \text{ kg m}^{-2} \text{ h}^{-1}$ in a solution comparable to ocean water⁴⁵ (3.5 wt% NaCl) (Fig. 5b). As the salt concentration increases up to 10.0 wt% NaCl, the evaporation rate shows only a slight decline in performance, indicating its capability to operate not only on typical ocean water, but also on higher salinity brines without too considerable a drop in the evaporation rate. In addition, no salt accumulation was observed on the top surface of the desalinator during any of the saline evaporation rate tests. This strong performance in salt water owes itself to the excellent salt-rejection abilities of the leaf-guar desalinator, which are exemplified in Fig. 5c. In this experiment, 0.5 g of NaCl is deposited on the top surface of the leaf-guar desalinator while its bottom surface remains in contact with ocean water. The setup is kept at ambient temperature and pressure and sees no solar

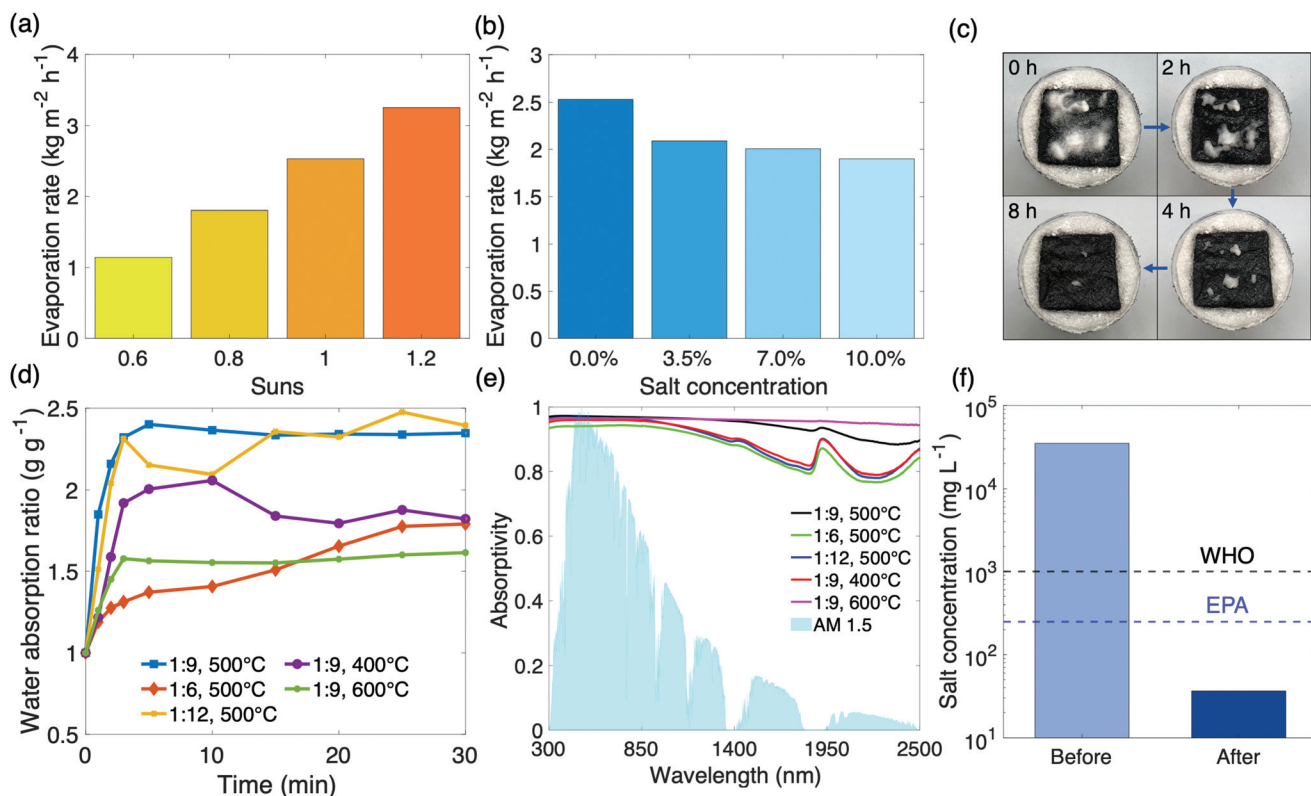


Fig. 5 Environmental variation, salt rejection and fabrication variation. Evaporation rate of leaf-guar desalinator (a) under various irradiance values, and (b) with various concentrations of saline water. (c) Salt-rejection ability of the leaf-guar desalinator. (d) Water absorption ratios and (e) absorptances of leaf-guar desalinators with various ratios of guar gum and several carbonization temperatures. (f) Salt concentration of ocean water obtained from Revere Beach, Massachusetts, before and after evaporation via the leaf-guar desalinator.

irradiation. Within 4 h, most of the desalinator surface is unobstructed by the salt, and after 8 h, barely any salt remains. The small amount of salt remaining after 8 h is fully rejected to the water supply after 11 h, as shown in Fig. S8†. While this does not represent especially rapid salt rejection, this level of performance would easily allow any accumulated salt to be rejected to the water supply over the course of one night (approximately 12 h), providing a clean top surface for continual solar absorption without any operator interaction. Furthermore, because no salt accumulates on this surface under 1 sun even for brines as high as 10.0 wt% NaCl, no issues with salt accumulation are anticipated for this leaf-guar desalinator.

Fig. 5d and e provide support for the selected fabrication guar ratios and carbonization temperatures. The water absorption ratios of samples carbonized at 400 °C and 600 °C are weaker than that of samples at 500 °C. Increasing the ratio of guar powder to filtered leaf from 1:9 to 1:6 also has a detrimental effect on the water absorption ratio. While the inclusion of the guar is essential for structural stability and endurance of the elevated carbonization temperatures, it also appears to limit the water absorption abilities of the desalinator. This is further supported by the data from the 1:12 ratio sample, which displays a water absorption ratio comparable to that of the standard 1:9 sample. While the 1:12 sample displays commensurate water absorption performance, its spectral absorbance is lacking in comparison with other samples. The chosen 1:9, 500 °C-carbonized sample displays a strong spectral absorbance in the solar irradiance wavelength region, second only to its 600 °C-carbonized counterpart. However, since the latter exhibited poor water absorption, it is not a suitable candidate for the desalinator. Thus, as the 1:9 sample carbonized at 500 °C boasts formidable water and solar absorbances as compared to samples with modified fabrication characteristics, it is identified as the strongest performer for a desalination device.

Evaporated water was also harvested using the leaf-guar desalinator in order to evaluate its salinity. Ocean water gathered from Revere Beach, Massachusetts was used as the starting solution for this test. Upon vaporization *via* this desalinator, water salinity decreases by three orders of magnitude – well below the maximum salinities for drinking water set by both the World Health Organization (WHO) and the Environmental Protection Agency (EPA) (1000 mg L⁻¹ and 250 mg L⁻¹, respectively^{46,47}).

Finally, to explicitly demonstrate the benefit of the leaf-guar desalinator within a solar evaporation system, an outdoor experiment is performed (Fig. S9†). Two identical evaporation chambers made from transparent polycarbonate (PC)⁴⁸ are used to construct the chambers. Both chambers are supplied with ocean water, and one chamber uses the leaf-guar desalinator to promote rapid evaporation. These chambers are placed on the rooftop of Snell Engineering Center at Northeastern University, Boston, MA, USA on September 3, 2021. Condensed fresh water is collected from both chambers after a test period of 6 h. The chamber employing the leaf-guar

desalinator devices yields approximately 3.40 times as much fresh water as the chamber with only water, illustrating the evaporation rate enhancement offered by this desalinator. Similarly, the 12 h averaged evaporation rate of the desalinator in fresh water determined earlier ($2.40 \text{ kg m}^{-2} \text{ h}^{-1}$) is approximately 3.33 times higher than that of the fresh water alone ($0.72 \text{ kg m}^{-2} \text{ h}^{-1}$). This indicates strong continuity between the lab and outdoor evaporation experiments, and provides further justification that this device will function well in salt water. As such, this leaf-guar desalinator, with its exceptional evaporation performance, is absolutely capable of helping to mitigate the global water crisis.

4 Conclusions

A desalination device composed entirely of biomass, incorporating both fallen tree leaves and guar, has been designed, characterized, and demonstrated within this work. A simple fabrication method is combined with renewable natural materials to realize a highly efficient evaporation rate of $2.53 \text{ kg m}^{-2} \text{ h}^{-1}$ for a single hour and $2.40 \text{ kg m}^{-2} \text{ h}^{-1}$ for an elongated exposure of 12 h under 1 sun. This performance is maintained *via* the well-established characteristics which constitute a strong solar desalinator, including exceptional solar absorbance, rapid water uptake, low thermal conductivity, and excellent salt rejection. These attributes also promote the versatility of the leaf-guar desalinator, enabling robust performance under a variety of solar irradiance values and in brines with concentrations as high as 10 wt% NaCl. The demonstration of these key performance metrics proves that this device is suitable for deployment as a practical desalination device, capable of efficiently producing fresh water in a variety of environments. This is further supported by an outdoor evaporation experiment, which clearly exemplifies the benefit of the leaf-guar desalinator in a practical use case.

Design choices and fabrication techniques which contribute to critical desalinator properties are discussed within this work as well. Special attention is paid to the effects of pyrolysis and chemical treatment on the porous structure and water absorbance capabilities of the material, due to significant transformations of these aspects throughout the fabrication process. This allows for the facile application of these methods to similar raw biomass and biowaste materials, supporting the creation of additional renewably-sourced evaporation devices. While guar itself is not a bio-waste product like fallen leaves, it can be incorporated within this desalinator design for less than \$12 per m², greatly complimenting the low cost of this device. Natural desalinators such as the leaf-guar device outlined herein have the capability to alleviate the global water crisis plaguing society in a sustainable manner. With such simple and cost-effective fabrication, large-scale production of such devices could provide relief to populations worldwide without simultaneously exacerbating the waste mismanagement crisis.

Author contributions

Andrew Caratenuto: conceptualization, methodology, validation, formal analysis, investigation, writing-original draft, visualization. Abdulrahman Aljwirah: conceptualization, methodology, validation, investigation, writing-review & editing. Yanpei Tian: conceptualization, investigation, writing-review & editing. Xiaojie Liu: conceptualization, investigation, writing-review & editing. Yinsheng Wan: conceptualization, writing-review & editing. Yi Zheng: conceptualization, resources, writing-review & editing, supervision, funding acquisition.

Conflicts of interest

There are no conflicts to declare.

Acknowledgements

The authors would like to thank Ying Mu and Dr. Marilyn L. Minus for conducting the mechanical bending experiment. This project is supported by the National Science Foundation through grant number CBET-1941743.

Notes and references

- 1 M. T. H. van Vliet, E. R. Jones, M. Florke, W. H. P. Franssen, N. Hanasaki, Y. Wada and J. R. Yearsley, *Environ. Res. Lett.*, 2021, **16**, 024020.
- 2 E. A. Adams, J. Stoler and Y. Adams, *Am. J. Hum. Biol.*, 2019, **32**, e23368.
- 3 F. Dolan, J. Lamontagne, R. Link, M. Hejazi, P. Reed and J. Edmonds, *Nat. Commun.*, 2021, **12**, 1915.
- 4 N. Ferronato and V. Torretta, *Int. J. Environ. Res. Public Health*, 2019, **16**, 1060.
- 5 Y. Chae and Y.-J. An, *Environ. Pollut.*, 2018, **240**, 387–395.
- 6 A. Alkaisi, R. Mossad and A. Sharifian-Barforoush, *Energy Procedia*, 2017, **110**, 268–274.
- 7 J. Kim, K. Park, D. R. Yang and S. Hong, *Appl. Energy*, 2019, **254**, 113652.
- 8 U. Caldera and C. Breyer, *Water Resour. Res.*, 2017, **53**, 10523–10538.
- 9 M. Walschot, P. Luis and M. Liegeois, *Water Int.*, 2020, **45**, 112–124.
- 10 H. Liu, Z. Huang, K. Liu, X. Hu and J. Zhou, *Adv. Energy Mater.*, 2019, **9**, 1900310.
- 11 P. Tao, G. Ni, C. Song, W. Shang, J. Wu, J. Zhu, G. Chen and T. Deng, *Nat. Energy*, 2018, **3**, 1031–1041.
- 12 G. Ni, S. H. Zandavi, S. M. Javid, S. V. Boriskina, T. A. Cooper and G. Chen, *Energy Environ. Sci.*, 2018, **11**, 1510–1519.
- 13 L. Zhang, Z. Xu, L. Zhao, B. Bhitia, Y. Zhong, S. Gong and E. N. Wang, *Energy Environ. Sci.*, 2021, **4**, 1771–1793.
- 14 J. Chen, J. L. Yin, B. Li, Z. Ye, D. Liu, D. Ding, F. Qian, N. V. Myung, Q. Zhang and Y. Yin, *ACS Nano*, 2020, **14**, 17419–17427.
- 15 R. Chen, K. Zhu, Q. Gan, Y. Yu, T. Zhang, X. Liu, M. Ye and Y. Yin, *Mater. Chem. Front.*, 2017, **1**, 2620–2626.
- 16 Z. Chen, Q. Li and X. Chen, *ACS Sustainable Chem. Eng.*, 2020, **8**, 13850–13858.
- 17 I. Ibrahim, V. Bhoopal, D. H. Seo, M. Afsari, H. K. Shon and L. D. Tijing, *Mater. Today Energy*, 2021, **21**, 100716.
- 18 P. Qiu, F. Liu, C. Xu, H. Chen, F. Jiang, Y. Li and Z. Guo, *J. Mater. Chem. A*, 2019, **7**, 13036–13042.
- 19 Q. Zhang, X. Xiao, G. Zhao, H. Yang, H. Cheng, L. Qu, W. Xu and X. Wang, *J. Mater. Chem. A*, 2021, 10945–10952.
- 20 N. Xu, X. Hu, W. Xu, X. Li, L. Zhou, S. Zhu and J. Zhu, *Adv. Mater.*, 2017, **29**, 1606762.
- 21 Y. Shi, Y. Ge, J. Chang, H. Shao and Y. Tang, *Renewable Sustainable Energy Rev.*, 2013, **22**, 432–437.
- 22 G. Yang, Y. Hu and J. Wang, *Bioresour. Technol.*, 2019, **285**, 121342.
- 23 L. N. Liew, J. Shi and Y. Li, *Bioresour. Technol.*, 2011, **102**, 8828–8834.
- 24 H. Li, F. Shen, W. Luo, J. Dai, X. Han, Y. Chen, Y. Yao, H. Zhu, K. Fu, E. Hitz and L. Hu, *ACS Appl. Mater. Interfaces*, 2016, **8**, 2204–2210.
- 25 K. Hong, L. Qie, R. Zeng, Z. Yi, W. Zhang, D. Wang, W. Yin, C. Wu, Q. Fan, W. Zhang and Y. Huang, *J. Mater. Chem. A*, 2014, **2**, 12733–12738.
- 26 D. Mudgil, S. Barak and B. S. Khatkar, *J. Food Sci. Technol.*, 2014, **51**, 409–418.
- 27 Y. Tian, X. Liu, J. Li, Y. Deng, J. A. DeGiorgis, S. Zhou, A. Caratenuto, M. L. Minus, Y. Wan, G. Xiao and Y. Zheng, *Cell Rep. Phys. Sci.*, 2021, 100549.
- 28 Y. Gokce and Z. Aktas, *Appl. Surf. Sci.*, 2014, **313**, 352–359.
- 29 NREL, *Reference Air Mass 1.5 Spectra*, <https://www.nrel.gov/grid/solar-resource/spectra-am1.5.html>.
- 30 M. Sevilla and A. B. Fuertes, *Carbon*, 2009, **47**, 2281–2289.
- 31 J. Cao, G. Xiao, X. Xu, D. Shen and B. Jin, *Fuel Process. Technol.*, 2013, **106**, 41–47.
- 32 A.-N. A. El-Hendawy, *J. Anal. Appl. Pyrolysis*, 2006, **75**, 159–166.
- 33 K. Ishimaru, T. Hata, P. Bronsveld, D. Meier and Y. Imamura, *J. Mater. Sci.*, 2007, **42**, 122–129.
- 34 Z. Song-lin, G. Shang-yu, Y. Xi-gen and X. Bo-sen, *J. For. Res.*, 2003, **14**, 75–79.
- 35 G. K. Parshteti, S. K. Hoekman and R. Balasubramanian, *Bioresour. Technol.*, 2013, **135**, 683–689.
- 36 H. Zhang, C. Dou, L. Pal and M. A. Hubbe, *BioResources*, 2019, **14**, 7494–7542.
- 37 F. P. Incropera, D. P. DeWitt, T. L. Bergman and A. S. Lavine, *Fundamentals of Heat and Mass Transfer*, Wiley, Hoboken, NJ, 6th edn, 2007.
- 38 Q. Fang, T. Li, Z. Chen, H. Lin, P. Wang and F. Liu, *ACS Appl. Mater. Interfaces*, 2019, **11**, 10672–10679.
- 39 X. Shan, A. Zhao, Y. Lin, Y. Hu, Y. Di, C. Liu and Z. Gan, *Adv. Sustainable Syst.*, 2020, **4**, 1900153.
- 40 C. Zhang, B. Yuan, Y. Liang, L. Yang, L. Bai, H. Yang, D. Weig, F. Wang, Q. Wang, W. Wang and H. Chen, *Mater. Chem. Phys.*, 2021, **258**, 123998.
- 41 X. Zhang, L. Yang, B. Dang, J. Tao, S. Li, S. Zhao, W. Li, J. Li, Z. Chen and S. Liu, *Nano Energy*, 2020, **78**, 105322.

- 42 I. S. Oh, J. I. Kim, J. K. Kim, K. W. Kim and H. J. Joo, *J. Mater. Sci.*, 1999, **34**, 4585–4595.
- 43 F. Zhao, X. Zhou, Y. Shi, X. Qian, M. Alexander, X. Zhao, S. Mendez, R. Yang, L. Qu and G. Yu, *Nat. Nanotechnol.*, 2018, **13**, 489–495.
- 44 J. A. Duffie and W. A. Beckman, *Solar Engineering of Thermal Processes*, Wiley, Hoboken, NJ, 4th edn, 2013.
- 45 C. Wunsch, *Quat. Sci. Rev.*, 2016, **135**, 154–170.
- 46 WHO, *Guidelines for Drinking-Water Quality*, 1996.
- 47 EPA, EPA 816-F-09-004, 2009.
- 48 X. Liu, Y. Tian, Y. Wu, A. Caratenuto, F. Chen, S. Cui, J. A. DeGiorgis, Y. Wan and Y. Zheng, *J. Mater. Chem. A*, 2021, DOI: 10.1039/D1TA05068K.